

## Experimental and Numerical Study on Anchorage Strength and Deformation Properties of Blocky Rock Mass

Junfu Zhu<sup>1</sup>, Qian Yin<sup>1,2,\*</sup>, Hongwen Jing<sup>1</sup>, Xinshuai Shi<sup>1</sup> and Minliang Chen<sup>1,3</sup>

<sup>1</sup>State Key Laboratory for Geomechanics and Deep Underground Engineering, China University of Mining and Technology, Xuzhou, 221116, China

<sup>2</sup>State Key Laboratory of Geohazard Prevention and Geoenvironment Protection, Chengdu University of Technology, Chengdu, 610059, China

<sup>3</sup>JSTI Group, Nanjing, 210000, China

\*Corresponding Author: Qian Yin. Email: yinq0104@cumt.edu.cn

Received: 07 July 2020; Accepted: 17 August 2020

**Abstract:** This study experimentally and numerically investigated the anchorage properties, bolt force evolution, deformation and stress fields of blocky rock mass with various dip angles of joint surfaces under an applied axial load. The results show that due to bolt reinforcement, the axial stress-strain curves of anchorage blocky rock mass show typical strain-hardening characteristics, and compared with models without anchorage, the peak strength and elastic modulus increase by 21.56% and 20.0%, respectively. With an increase in axial stress, the lateral strain continuously increases, and restriction effects of bolts reduce the overall deformation of model surfaces. The axial stress-strain curves of anchorage blocky rock mass in the simulations present a “double peak strength” phenomenon due to bolt reinforcement, and the peak strength, second peak strength, residual strength, surface displacement field, as well as the principal stress fields all depend on the dip angles of joint surfaces. As a result of the bolt reinforcement effects, cone-shaped compression zones are produced in the models, and compression zones of adjacent bolts superimpose with each other to form anchorage belts, improving the overall bearing capacity of anchorage models. Obvious stress concentration can be observed at both bolt end and anchorage section. Not only the role of bolt support transfers the blocky rock mass to be a three-dimensional stress state through compression effects, but also it improves both tensile strength and shear resistance of both joint surfaces and the overall blocky rock mass.

**Keywords:** Blocky rock mass; anchorage; strength; displacement; numerical simulation

### 1 Introduction

During a long geological period, due to the influences of geological tectonic movements, natural weathering and human activities, the sedimentary rock mass usually develops various geological defects, such as joints, beddings, faults and weak interlayers, to become complicated blocky rock mass [1–7]. Under an applied load, development and coalescence of these defects



This work is licensed under a Creative Commons Attribution 4.0 International License, which permits unrestricted use, distribution, and reproduction in any medium, provided the original work is properly cited.

change the structures and stress conditions of rock mass, resulting in slide, falling, fracture and instability of rock projects [8–11]. Thus, it is of great significance to investigate the mechanical properties of blocky rock mass to ensure stability and safety of rock projects [12–14].

Until recently, a lot of studies have been conducted to study the strength and deformation properties of joint rock mass containing weak interlayers [15–17]. Yin et al. [2] conducted a series of experiments to study the mechanical properties and anchorage performances of rock mass in the fault fracture zone, and the results show that the ultimate failure modes of anchored models are characterized by cracks propagating along the cementing surfaces. Zhang et al. [18] investigated mechanisms of shear deformation, failure and energy dissipation of joints using both physical and numerical direct shear tests under constant normal load condition. The results show that joints under shearing present a dissipation trend of four stages including a slow rise, a rapid rise, a shock rise and a rapid decline stage, respectively. Wang et al. [19] analyzed the correlation of the friction angle with the normal stress level to overcome overestimation or underestimation at relatively low or high normal stress levels in the JRC-JCS empirical model, and the modified nonlinear shear criterion was proposed. Yang et al. [20] proposed a damage model which considers the influence of normal vector and area density of joints to describe the discontinuities, and the displacements and damage zones in the surrounding rock mass of an underground cavern were predicted. Wang et al. [21] carried out uniaxial compression tests to investigate the influences of pre-existing fissure geometry parameters (various dip angles, lengths, widths, and numbers) on mechanical properties and deformation failure models of low-strength rock samples. The above researches on mechanical properties of joint rock mass will provide benefit guidance for our study. However, when it comes to blocky rock mass, few studies have been reported.

For decades, rock bolts have been extensively applied as the primary elements to support rock masses with geological defects in geotechnical and mining projects [2,22,23]. Zhu et al. [24] conducted a number of indoor model tests to obtain a better understanding of the failure behaviors and anchoring effects of a weak-broken rock slope. The results indicate that the bolt reinforcements not only improve vertical bearing capacity before failure but also reduce the vertical settlement and allow greater lateral deformation. Li et al. [25] investigated the mechanical properties, anchorage effects, cracking, and coalescence process of rock mass containing flaws. The results show that both the number of rock bolts and the anchoring angle have a great influence on the anchorage effect, and three types of failure characteristics have been systematically analyzed. Wu et al. [26] performed a series of cyclic shear tests on bolted rock joints, and the results present that the cyclic displacement has an influence on failure modes of rock bolts, and the influence of cyclic loading on the shear resistance of the rock bolt is more significant than its counterpart of the rock bolt itself, and the shear performance of a rock bolt is strongly affected by cyclic shear loading. However, for blocky rock mass with various dip angles of joint surfaces, the anchorage strength and deformation properties have rarely been investigated.

Therefore, in this study, the anchorage properties of blocky rock mass were experimentally and numerically studied. First, evolution characteristics of the axial stress, lateral stress, bolt force and ultimate failure modes of anchorage blocky rock mass were experimentally investigated. Furthermore, by using the discrete element method 3DEC, a large number of simulations on variations in the axial stress-strain curves, elastic modulus, peak strength, second peak strength, residual strength, displacement contours and maximum principal stress fields were respectively studied. Finally, the anchorage mechanism of rock bolt support to blocky rock mass was discussed. The findings might have a theoretical significance for stability evaluation and support

parameter design of geotechnical projects with blocky rock mass, such as mining, tunneling and rock slopes.

## 2 Model Test on Anchorage Mechanical Properties of Blocky Rock Mass

### 2.1 Research Background

The typical outcrop blocky rock mass in Jining coal mine area, Shanxi Province, China, was taken as the research background in this study. For the convenience of mine construction, coal and slag transportation, and miners' living needs, a winding mountain road was reclaimed, and blocky rock mass on the slope was exposed, as shown in Fig. 1. The natural stress state of rocks in the open pit slope can be described as follows. Due to excavation, stress relief happens to the rock slope, and the stress state transfers to a 2D stress state, accompanied with expansion deformation of the free surface. Thus, collapse and falling stone are frequent geological hazards here. In order to prevent rockfall hazards, grouting bolts, accompanied with steel belts, were installed on the slope to make the rock slope return to a 3D stress state. The schematic diagram is displayed in Fig. 2. Due to bolt reinforcement, blocky rock mass of the slope was transformed into three-dimensional stress states again, shown as the mechanical unit in Fig. 2. Note that, for sedimentary rock mass, the joint surfaces were generally parallel at the beginning, but due to the influences of crustal movement, human disturbance, and natural weathering, the joints were gradually staggered, resulting in complex joint networks dividing the rock mass (Fig. 2).

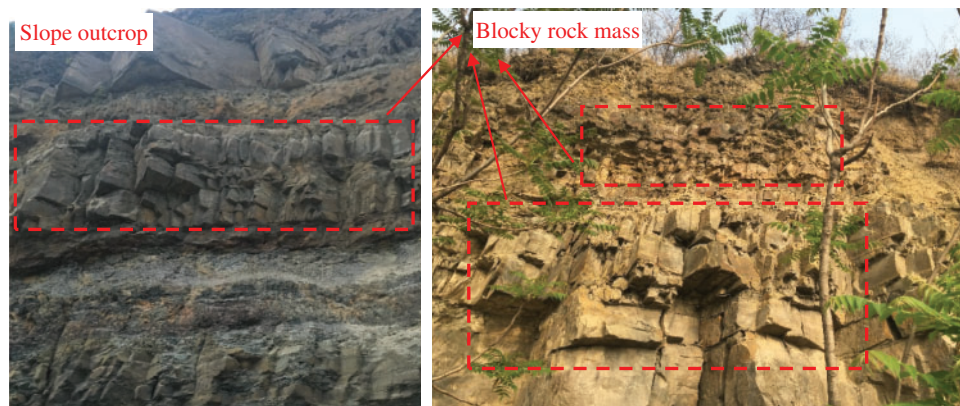


**Figure 1:** Typical outcrop blocky rock mass of Jining coal mine area

### 2.2 Experiment Model Preparation

In the experiment, cubic models with the side length of 200 mm were prepared. The real bolt length in site is 2000 mm, thus the geometric similarity ratio  $C_L$  is 10 due to the bolt in the experiment runs through the whole model thickness. The mixture of C32.5 ordinary portland cement, gypsum and water was chosen as the cementing materials, and well-graded clean river sand was chosen as the aggregate. The unit weight  $\gamma_m$  of similar materials for the rock matrix is  $16.5 \text{ kg/m}^3$ , and the real in situ sandy mudstone has a unit weight  $\gamma_p$  of  $23.1 \text{ kg/m}^3$ . Thus, the unit weight similarity ratio  $C_\gamma = \gamma_p/\gamma_m = 23.1/16.5 = 1.40$ , and the strength similarity ratio  $C_R = C_\gamma C_L = 10 \times 1.40 = 14.0$ . The uniaxial compressive strength, tensile strength, elastic modulus, Poisson's ratio, and average unit weight of the real rock are listed in Tab. 1. Then, through conducting a large number of uniaxial compression, Brazilian splitting and variable angle

shear tests on the similar materials, the mass ratio  $\lambda_1$  of sand:cement:gypsum:water = 3:0.7:0.3:0.5 was finally chosen to simulate the real rock matrix. The results present that the simulated uniaxial compressive strength  $\sigma_{cm}$ , elastic modulus  $E_m$ , tensile strength  $\sigma_{tm}$ , cohesion force  $c_m$  and internal friction angle  $\phi_m$  of rock matrix are 4.75 MPa, 1027.23 MPa, 0.71 MPa, 1.98 MPa and  $25.32^\circ$ , respectively, as shown in Tab. 1. Based on the results of some previous studies [27–29], the structural planes were prefabricated by mixing gypsum, silicon powder and water with a mass ratio  $\lambda_2$  of 1:1:0.5, and the cohesion force  $c_j$  and internal friction angle  $\phi_j$  are 0.059 MPa and  $43.67^\circ$ , respectively. The aluminium bar with the diameter of 6 mm was chosen to simulate the real bolt, with strain gauge pasted in the middle position. The steel belt is of strip shape, with the size of 190 mm  $\times$  30 mm  $\times$  0.4 mm, and the tray is also made of steel with the size of 20 mm  $\times$  20 mm  $\times$  1.5 mm.

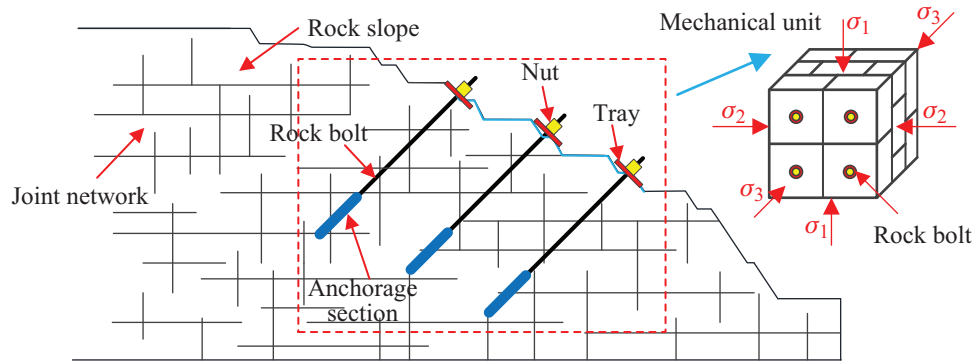


**Figure 2:** Schematic diagram of blocky rock slope with bolt support

**Table 1:** Physical and mechanical parameters of both real rock and the model

	Uniaxial compressive strength/MPa	Tensile strength/MPa	Elastic modulus/GPa	Poisson's ratio	Unit weight/kg $\cdot$ m $^{-3}$
Real rock	40~70	7.0~11.0	13~25	0.22	23.1
Model	2.86~5.0	0.50~0.79	0.93~1.79	0.22	16.5

The fabrication process of the blocky rock mass is shown in Figs. 3a–3f. In order to easily demould, a layer of release agent was first applied on the inner walls of the mould. Then, the cement, gypsum, sand and water were weighed in proportion respectively, mixed, and stirred evenly (Fig. 3a). Then the similar materials were poured into the mould. To set the joint surfaces and bedding planes, the model was poured layer by layer using the moulds of cross frame shape, and to ensure the homogeneity of model, the vibration of 2–3 min was conducted for each layered pouring, as shown in Fig. 3b. After initial solidification, the frames were taken out, and the mixed slurry of gypsum and silicon powder was poured to produce the joint surfaces and bedding planes with a spacing of 10 mm and 5 mm respectively (Figs. 3c–3f). When the blocky rock mass was readily prepared, end surfaces of the models were polished, and then four bolt holes were drilled through the whole thickness of models using a hand-operated electric drill with the diameter of

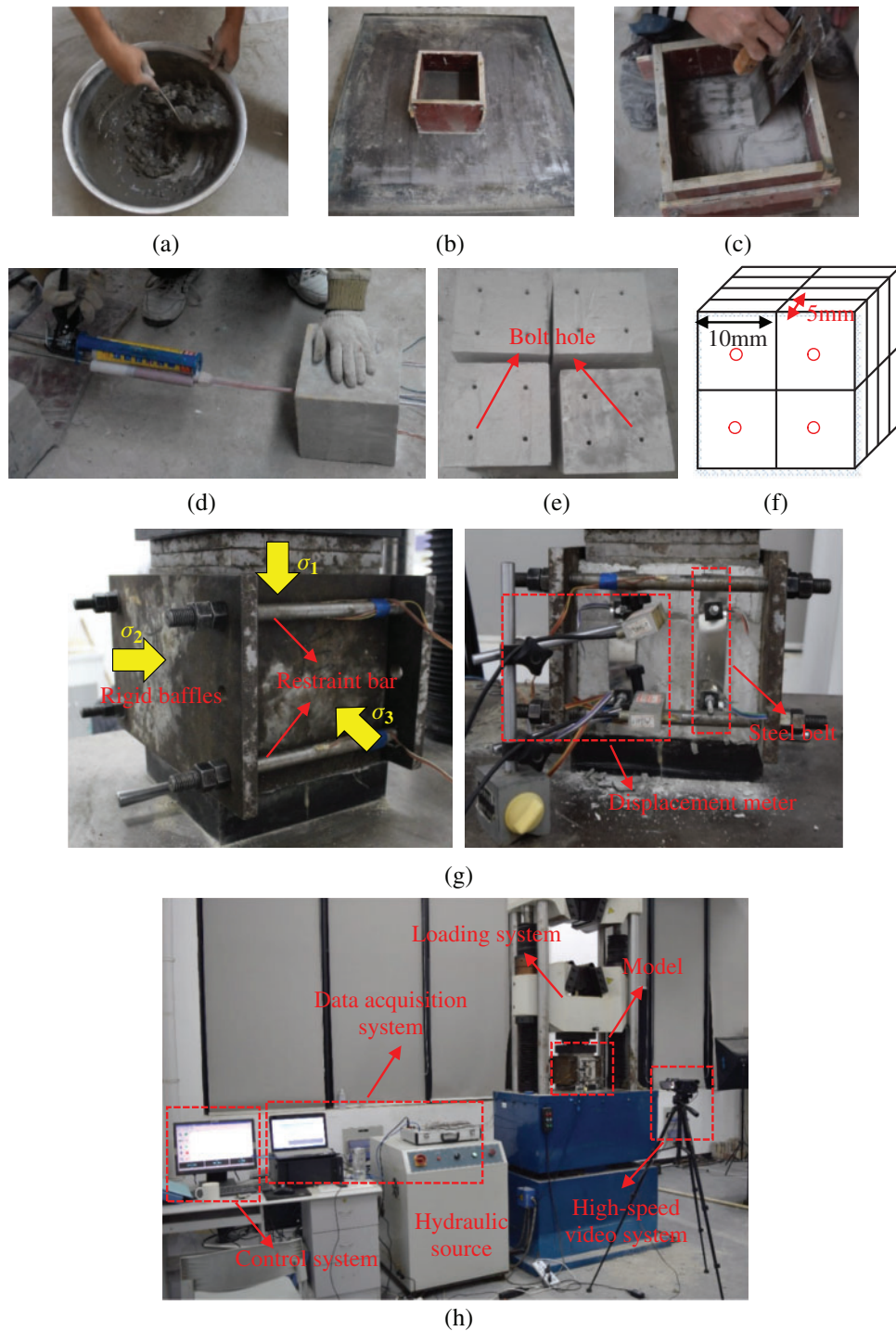
7 mm (Fig. 3d). Finally, the models were air dried for 24 h (Fig. 3e), with the model diagram displayed in Fig. 3f.

The constrained system of the model is shown in Fig. 3g. In the engineering site, due to excavation of rock slope, stress relief happens to the working face, resulting in variations in the natural stress state and corresponding expansion deformation. To prevent rockfall and slope slip hazards, rock bolts with steel belts were chosen as the supports. Therefore, in accordance with the natural stress and deformation conditions of the anchorage blocky rocks in situ, rigid baffles and restraint bars were used to provide displacement constraints, and the boundary equipped with the supports of bolt and steel belt was the corresponding deformation free surface. The axial stress  $\sigma_1$  was applied using the YNS-2000 rock mechanics testing system with a constant strain rate of 0.2 mm/min [30–32] (Fig. 3h), and  $\sigma_3$  was realized by the bolt and steel belt reinforcement. Note, the size of loading plate (20 mm  $\times$  20 mm) of the testing system is same as the boundary size of the model, which satisfies the full-scale stress conditions of the rock slope. In the test, after the bolt was installed, the epoxy typed planting bar glue was chosen as the anchoring agent, and steel belts and nuts were installed at the bolt end of the free surface, accompanied with steel trays. During the uniaxial compression of blocky rock mass, the axial and surface displacements were recorded using the testing system and displacement meters, respectively (Fig. 3g). The axial stress was real-time measured using the YNS-2000 rock mechanics testing system. The axial force of bolt was calculated based on the strain captured by the strain gauges, with an accuracy of  $\pm 2\%$ , and the free surface deformation of the model was measured using the displacement meters, with the accuracy of  $\pm 0.1\%$  F.S. The signals of both strain gauges and displacement meters were captured by the TST3826F dynamic and static strain acquisition system. Besides, a high-speed camera was applied to capture the real-time deformation and failure process of the models.

### 2.3 Experiment Results Analysis

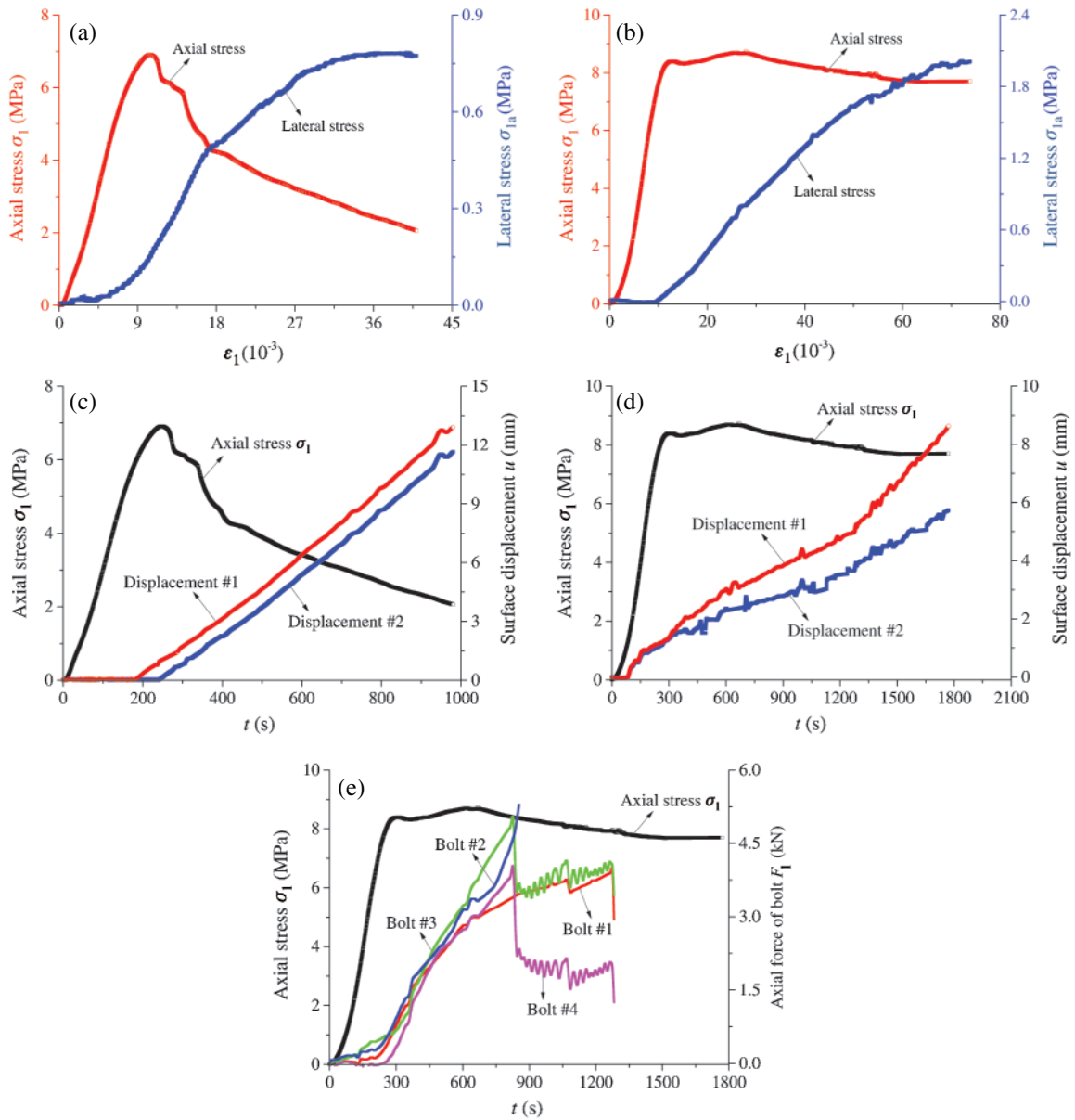
Figs. 4a–4b show the axial stress-axial strain and lateral stress-axial strain curves of blocky rock mass with/without anchoring under uniaxial compression, respectively. It can be seen that, for the model without anchorage, the axial stress  $\sigma_1$  declines gradually after the peak strength  $\sigma_{1c}$ , indicating typical strain-softening characteristics, but for the anchorage model, the axial stress fluctuates within a certain range, implying strain-hardening characteristics, and two peak stress points can be observed. As a result of the bolt reinforcement, the peak strength and elastic modulus show an increase by 21.56% and 20.0%, respectively. With increasing axial strain, the variations in lateral stress can be divided into three stages, i.e., basically no increase, rapid increase, and declining increase rate to stable values. The surface displacements of rock mass with/without anchorage show a significant difference. Generally, the restriction effect of bolts declines the deformation of model surfaces (Figs. 4c–4d).

Fig. 4e shows the evolution process of bolt force during the uniaxial compression. At the initial loading stage, the bolt force  $F_1$  presents a relatively slow growth. At  $t = 250$  s, the axial stress  $\sigma_1 = 7.91$  MPa = 94.17%  $\sigma_{1c}$ , the bolt force begins to increase. At  $t = 440$  s, the axial stress reaches the peak strength  $\sigma_{1c}$ , and the axial force  $F_1$  of bolt #1, #2, #3 and #4 is 1.91 kN, 2.07 kN, 2.07 kN and 1.85 kN, respectively. Then, with increasing axial stress, the axial force of bolt becomes larger. At  $t = 830$  s,  $\sigma_1 = 8.39$  MPa = 99.88%  $\sigma_{1c}$ , the axial force  $F_1$  of bolt #2, #3 and #4 reaches the peak values of 5.29 kN, 4.81 kN and 3.78 kN, respectively. Then, the strain gauge on bolt #2 damages. The axial force  $F_1$  of bolt #3 and #4 drops significantly and then fluctuates before the strain gauges damages. At  $t = 1060$  s,  $\sigma_1 = 8.10$  MPa = 96.43%  $\sigma_{1c}$ , the strain gauge on bolt #1 damages, accompanied with a significant axial force drop.



**Figure 3:** Experimental model preparation, constrained system and loading system. (a) Stirring. (b) Vibration. (c) Joint surface arrangement. (d) Bolt hole drilling. (e) Air drying. (f) Model diagram. (g) Constrained system. (h) YNS-2000 rock mechanics testing system

Ultimate failure modes of blocky rock mass with/without anchorage are displayed in Figs. 4f–4g. For the boundary with bolt, secondary cracks of the anchorage model are more developed due to stress concentration near the bolt. However, for the side boundary of models, compared with the model without anchorage, the number of cracks decreases and the crack aperture also declines due to the bolt reinforcement. For the model without anchorage, the ultimate failure mode presents a typical tensile failure along the joint surfaces or bedding planes, accompanied with several shear cracks, but for the anchorage models, a shear failure of “X” shape can be observed as a result of the three dimensional stress state in the model.



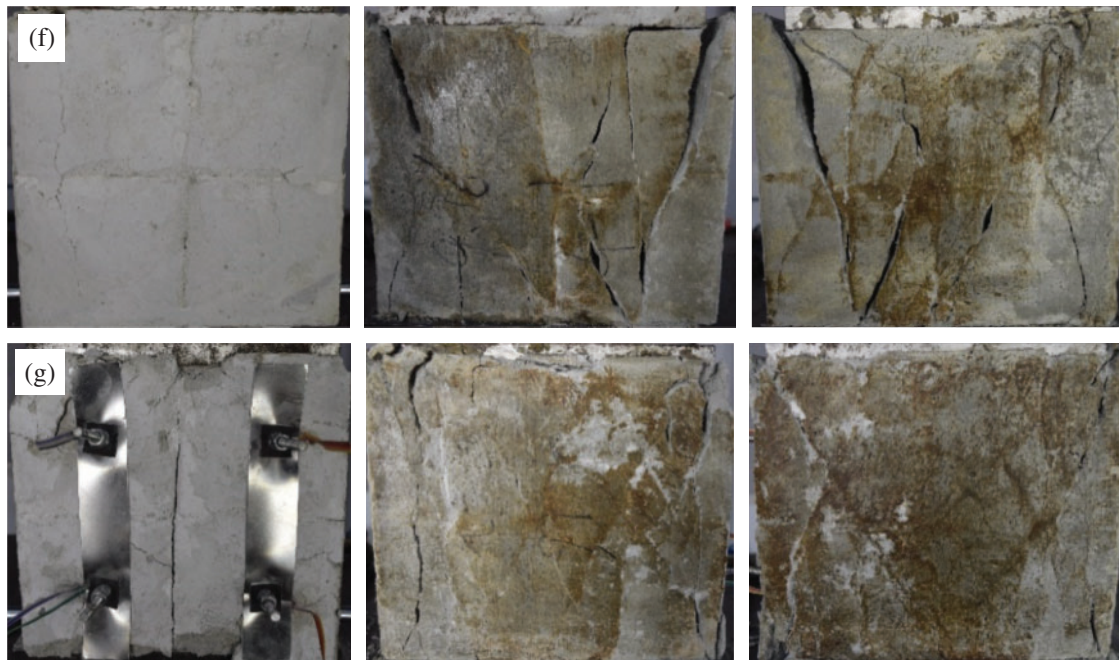


**Figure 4:** Evolution of axial stress, lateral stress, surface displacement, bolt axial force and ultimate failure modes of models with/without anchoring

### 3 Numerical Analysis on Anchorage Mechanical Properties Using 3DEC

Due to the non repeatability, heavy workload and heterogeneity of large scale experiments for investigating the anchorage properties of blocky rock mass, and to study the evolution characteristics of internal stress and deformation fields, the discrete element method (DEM), which was initially developed as a two-dimensional representation of jointed rock masses, has been extended to the application of particle flow studies, micro mechanism studies of granular materials, and the crack development in rock masses. In DEM, the rock mass is considered as a group of discrete blocks bonded with each other along the joints. These joints allow the blocks to move and rotate, and individual blocks are regarded as a rigid or deformable material. The deformable blocks are subdivided into a series of finite-difference elements, and the mechanical response of each element conforms to the prescribed linear or nonlinear stress-strain law. The motion of joints in normal or shear directions is also controlled by linear or non-linear force-displacement relations. The dynamic relaxation algorithm is adopted to solve the systems of equations and the development of large displacements is allowed as the failure occurs [33,34]. In this study, the 3DEC discrete element numerical calculation software, which has the features of (1) allow limited displacements and rotations, including complete separation, and (2) automatic identification of new contacts during the calculation, was applied to reveal the anchorage mechanical behaviors of blocky rock mass under an applied axial load [35,36].

#### 3.1 Model Setup and Boundary Conditions

Based on the experimental model built above, cubic numerical models with the size of 200 mm × 200 mm × 200 mm were established using the 3DEC, and four bolts with trays and steel belts were added, with the pretightening bolt force of 0, as shown in Fig. 5a. Similar to the

experiment, the upper/lower boundaries (vertical to  $z$  axis) were loading surfaces. The boundary #1 vertical to  $y$  axis was a free surface, and the opposite boundary was displacement constrained. The left two boundaries (vertical to  $x$  axis) were bolt reinforced.

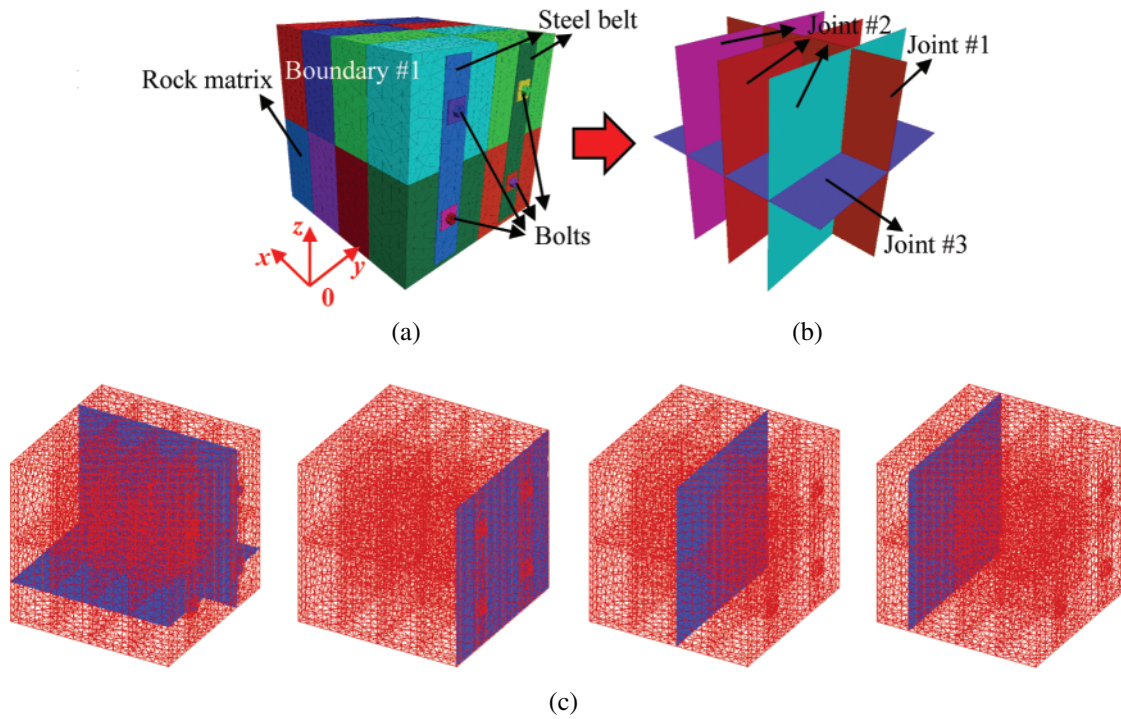


**Figure 5:** Numerical model building and monitoring surfaces. (a) Numerical model. (b) Joint surface. (c) Monitoring surfaces

From Fig. 5b, there are three different joint groups in the model, joint #1, joint #2 and joint #3, parallel to the  $x0z$ ,  $y0z$ , and  $x0y$  surfaces, respectively. In the numerical simulation, five monitoring sections were respectively selected to investigate the deformation and stress evolution characteristics during the loading process, as shown in Fig. 5c.

In the simulation, the strain-softening model was chosen as the constitutive model. This model is based on the UDEC Mohr–Coulomb model with nonassociated shear and associated tension flow rules. In the Mohr–Coulomb model, the cohesion, friction, dilation and tensile strength are assumed to remain constant, while in the strain-hardening/softening model, these properties may harden or soften after the onset of plastic yield. The yield and potential functions, plastic flow rules and stress corrections are identical to those of the Mohr–Coulomb model, as shown in Fig. 6. The following Mohr–Coulomb yield functions were utilized to failure envelope from point A to point B:

$$f^s = \sigma_1 - \sigma_3 N_\varphi + 2c\sqrt{N_\varphi} \tag{1}$$

$$N_\varphi = (1 + \sin \varphi)/(1 - \sin \varphi) \tag{2}$$



the experimental and numerical peak strength  $\sigma_{1c}$  is 8.73 and 8.47 MPa, respectively, with the deviation value  $\xi$  (ratio of difference to the average value) of 3.09%, and the experimental and numerical residual strength  $\sigma_r$  is 7.70 and 8.47 MPa, with the deviation value  $\xi$  of 9.49%. For the blocky rock mass without anchorage, the experimental and numerical  $\sigma_{1c}$  is 6.91 and 8.08 MPa, with the deviation value  $\xi$  of 2.45%. The above analysis implies that, the micro input parameters chosen in the numerical simulation can well reflect the macro mechanical responses of the anchorage blocky rock mass under an applied axial load.

**Table 2:** Micro input parameters of the numerical model

	Density (kg/m <sup>3</sup> )	Normal stiffness $K_n$ (GPa/m)	Bulk modulus $K$ (Pa)	Shear stiffness $K_s$ (Pa/m)	Cohesion force $c$ (Pa)	Tensile strength $\sigma_t$ (Pa)	Internal friction angle $\varphi$ (°)
Rock matrix	2500	–	8.58e8	1e11	2.72e6	0.97e6	33.67
Joint surface	–	79.2	–	3.96e8	5.89e4	0.25e6	25.32

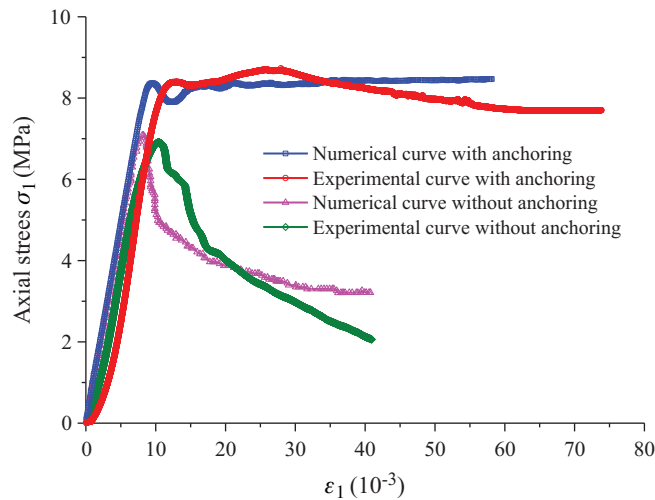


**Figure 7:** Comparison between numerical and experimental axial stress-strain curves

In the numerical study, in order to study the effects of joint surface angles on anchorage properties of blocky rock mass, there groups of numerical simulations were respectively conducted, as follows:

- (i) Various joint angle  $\alpha_1$  (0, 15, 30, 45, 60, 75, 90°).  $\alpha_1$  denotes the included angle between joint #3 and the  $x0y$  surface, as shown in Fig. 8a.
- (ii) Various joint angle  $\alpha_2$  (0, 15, 30, 45, 60, 75, 90°).  $\alpha_2$  denotes the included angle between joint #1 and the  $x0z$  surface, as shown in Fig. 8b.
- (iii) Various joint angle  $\beta_1$  (0, 15, 30, 45, 60, 75, 90°).  $\beta_1$  denotes the included angle between joint #2 and the  $y0z$  surface, as shown in Fig. 8c.

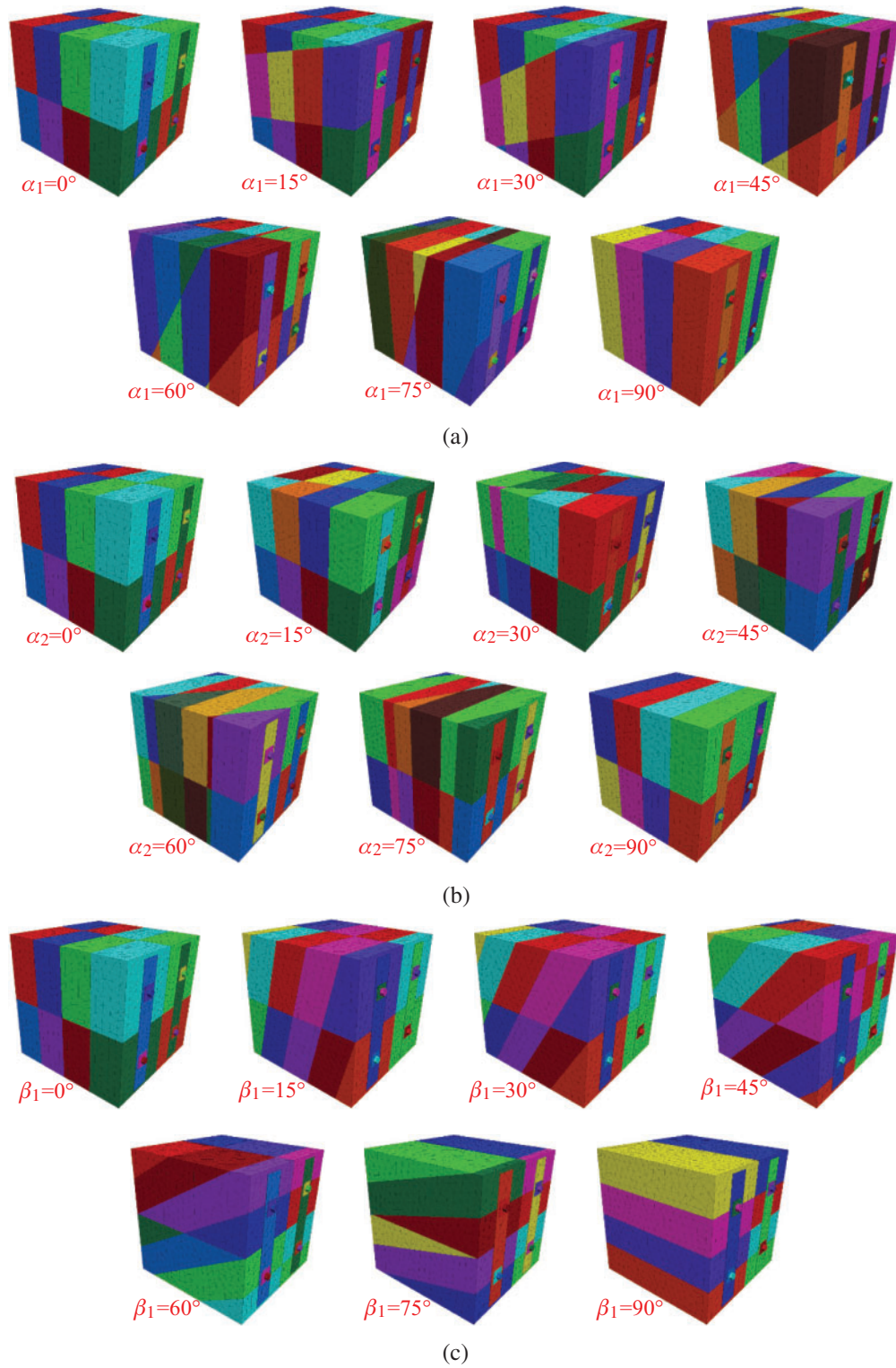


**Figure 8:** Numerical models with various  $\alpha_1$ ,  $\alpha_2$  and  $\beta_1$  values. (a) Various  $\alpha_1$ . (b) Various  $\alpha_2$ . (c) Various  $\beta_1$

### 3.2 Anchorage Properties of Blocky Rock Mass with Various $\alpha_1$

Fig. 9a presents the axial stress-strain curves of anchorage blocky rock mass with various  $\alpha_1$  values. It shows that the numerical curves do not present obvious initial compaction stages compared with the experimental results. Due to the anchorage effect of bolt, a “double peak strength points” phenomenon is produced. The axial stress-strain curves enter the plastic strain stage after the elastic deformation stage. After the peak strength point, the axial stress declines to the strain-softening stage. Then, after the second peak strength, the axial stress fluctuates in a small range and attains the residual strength.

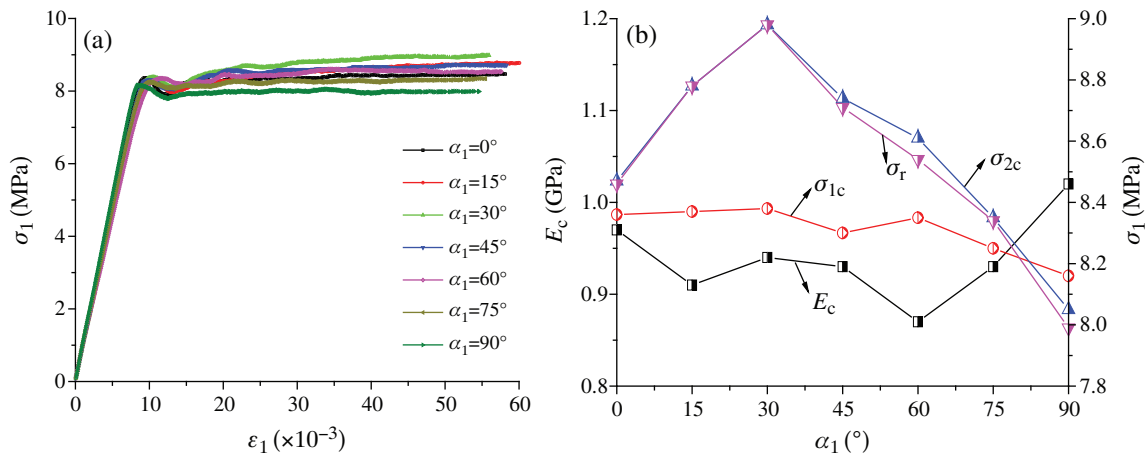


**Figure 9:** Axial stress-strain curves, elastic modulus and strength characteristics of the numerical models with various  $\alpha_1$  values

As  $\alpha_1$  increases from  $0^\circ$  to  $90^\circ$ , the elastic modulus  $E_c$  generally shows a variation of first decrease and then increase, reaching the minimum value of 0.87 GPa at  $\alpha_1 = 60^\circ$ . However, the peak strength  $\sigma_{1c}$ , second peak strength  $\sigma_{2c}$  and residual strength  $\sigma_r$  all present a first increasing and then decreasing variation trend, reaching the maximum values of 8.38 MPa, 8.98 MPa and 8.98 MPa, respectively, at  $\alpha_1 = 30^\circ$  (Fig. 9b).

After the uniaxial compression tests, variations in the average displacement contours were analyzed according to the monitoring surfaces (Fig. 5), as shown in Fig. 10. It can be seen that:

- (i) Due to compaction effects of the bolt, a cone-shaped anchorage compression zone is formed in the anchorage body, and the anchorage compression zones of adjacent bolts are superimposed with each other to generate a typical anchorage belt. The numerical results are consistent with some previous results [2,23,38–42]. The above analysis indicates that, the bolt can produce a stable cone-shaped compression zone by acting on the rock mass to improve the overall bearing capacity.
- (ii) With an increase in  $\alpha_1$ , change characteristics of the displacement for each monitoring surface present a similar variation, all indicating the maximum displacement between two bolts on the same steel belt. The deformation near the bolts and upper/lower model boundaries shows the smallest value. The bolt can restrain the surface deformation of the model obviously.

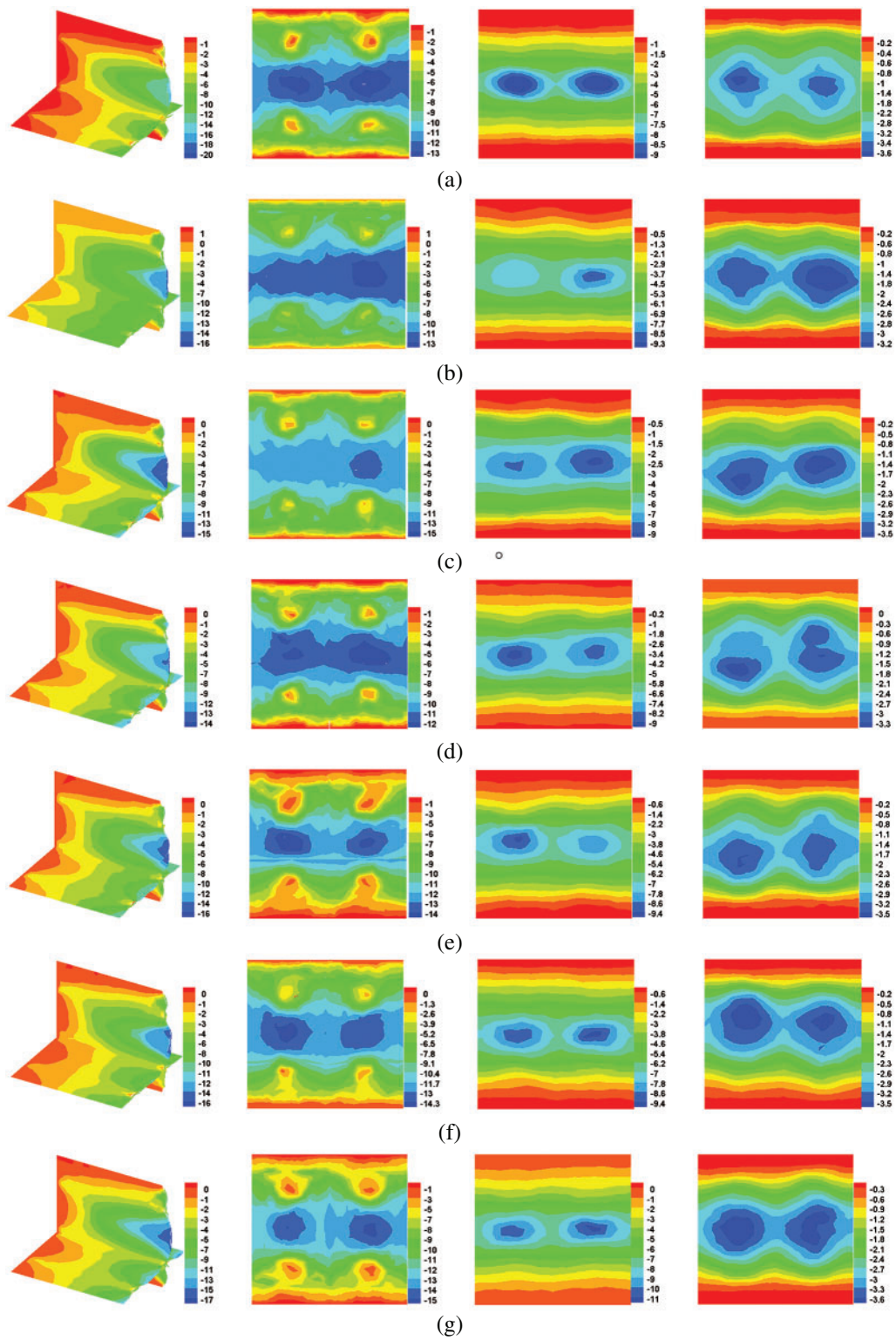


**Figure 10:** Displacement contours of the numerical models with various  $\alpha_1$  values. (a)  $\alpha_1 = 0^\circ$ . (b)  $\alpha_1 = 15^\circ$ . (c)  $\alpha_1 = 30^\circ$ . (d)  $\alpha_1 = 45^\circ$ . (e)  $\alpha_1 = 60^\circ$ . (f)  $\alpha_1 = 75^\circ$ . (g)  $\alpha_1 = 90^\circ$

- (iii) As  $\alpha_1$  increases from  $0^\circ$  to  $90^\circ$ , the average displacement on the model surfaces shows a first decreasing and then increasing variation, reaching the minimum value of 8.648 mm at  $\alpha_1 = 45^\circ$  (Fig. 11), which indicates that the overall bearing capacity of the anchorage blocky rock mass first increases and then decreases with increasing  $\alpha_1$  and verifies the variations in the strength properties displayed in Fig. 9b.

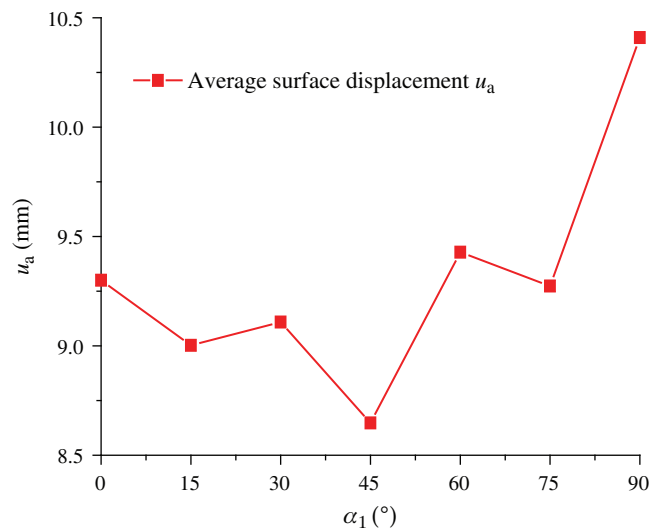


**Figure 11:** Variations in the average displacements of monitoring surfaces for the models with various  $\alpha_1$  values

Fig. 12 shows the changes in the maximum principal stress contours of the anchorage models with various  $\alpha_1$  values. It can be seen that:

- (i) Due to the two dimensional stress state on the model surface, the maximum principal stress is relatively low, and the stress at the joint position decreases obviously. However, due to the three dimensional stress state of the internal rock mass, the maximum principal stress is obviously large, and a stress concentration/decrease phenomenon can be observed at the joint positions. The above analysis indicates that the joints have a remarkable effect on the internal stress distribution as well as the mechanical properties.
- (ii) At the model surface, the maximum principal stress shows a great increase near the bolt position, but decreases obviously at the joint position, which indicates that the compaction effects of the bolt to the model is most obvious at the bolt position, and the anchorage effect gradually weakens far away from the bolt. The variations in the maximum principal stress are consistent with the deformation characteristics of the model.
- (iii) The anchorage effect of bolts disperses constantly along the bolt body direction, and tends to be uniform at the middle free section of the bolt. The weak plane of joints has a certain influence on the stress distribution in the model, and with increasing  $\alpha_1$ , the internal stress state varies, while the stress concentration and stress decrease still happen near the joint positions.

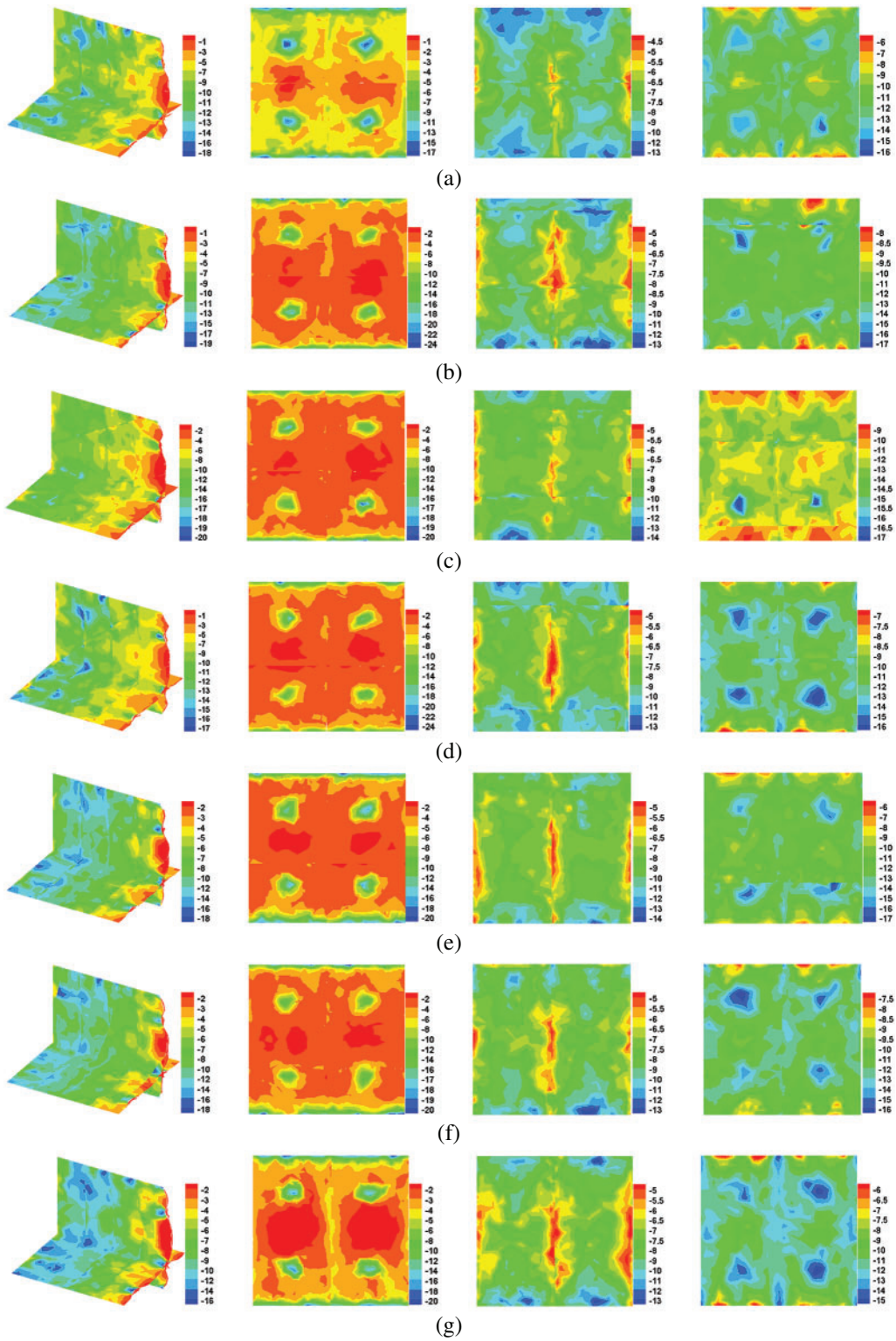


**Figure 12:** Maximum principal stress contours of the numerical models with various  $\alpha_1$  values. (a)  $\alpha_1 = 0^\circ$ . (b)  $\alpha_1 = 15^\circ$ . (c)  $\alpha_1 = 30^\circ$ . (d)  $\alpha_1 = 45^\circ$ . (e)  $\alpha_1 = 60^\circ$ . (f)  $\alpha_1 = 75^\circ$ . (g)  $\alpha_1 = 90^\circ$

### 3.3 Anchorage Properties of Blocky Rock Mass with Various $\alpha_2$

Fig. 13a presents the axial stress-strain curves of anchorage blocky rock mass with various  $\alpha_2$  values. The elastic deformation stage of all curves before the peak stress point is almost the same, while the post peak strain-softening stage, second peak strength, as well as the residual strength show a significant difference for the curves of blocky rock mass with various  $\alpha_2$  values.

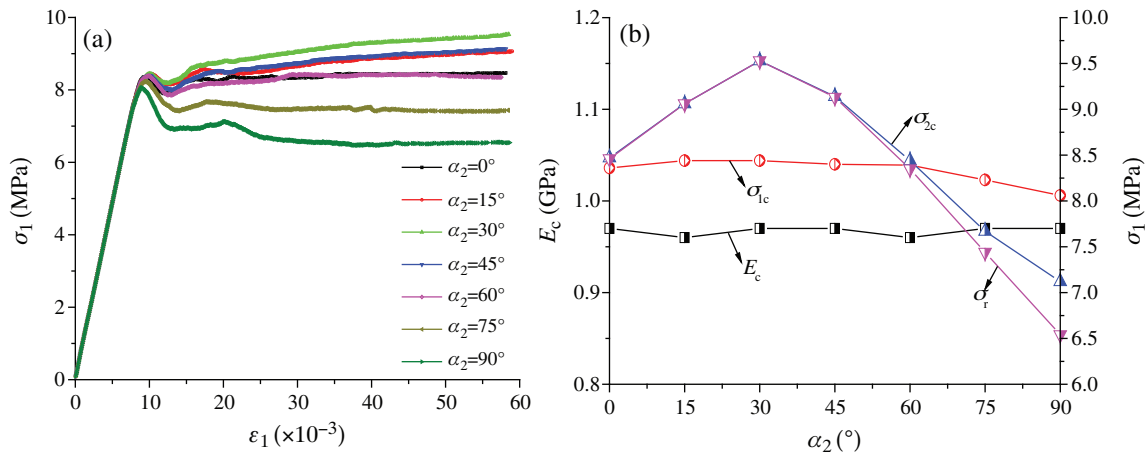


**Figure 13:** Axial stress-strain curves, elastic modulus and strength characteristics of the numerical models with various  $\alpha_2$  values

Variations in the mechanical properties of anchorage blocky models with an increase in  $\alpha_2$  are displayed in Fig. 13b. As  $\alpha_2$  increases, the elastic modulus  $E_c$  shows a little difference, fluctuating around 0.96 GPa, while the peak strength and residual strength change greatly. As  $\alpha_2$  increases from  $0^\circ$  to  $90^\circ$ , the peak strength, second peak strength and residual strength all first increase and then decrease, reaching the maximum values of 8.44 MPa, 9.53 MPa and 9.53 MPa, respectively, at  $\alpha_2 = 30^\circ$ . Variation extent of the peak strength  $\sigma_{1c}$  is small, while that for the second peak strength  $\sigma_{2c}$  is large. When  $\alpha_2$  is smaller than  $60^\circ$ , both the second peak strength  $\sigma_{2c}$  and residual strength  $\sigma_r$  are larger than the peak strength  $\sigma_{1c}$ , but for  $\alpha_2$  larger than  $60^\circ$ , both the second peak strength  $\sigma_{2c}$  and residual strength  $\sigma_r$  are smaller than the peak strength  $\sigma_{1c}$ .

Evolution characteristics of the displacement contours for the anchorage numerical models with increasing  $\alpha_2$  after uniaxial compression are displayed in Fig. 14. It can be seen that:

- (i) The maximum displacement of each monitoring section in the model is symmetrical at first, which is concentrated just below the steel belts. However, as  $\alpha_2$  increases, the maximum displacement contours shift gradually. The displacement under the left steel belt decreases, while the displacement under the right steel belt gradually transfers to the middle position. Then, with further increase in  $\alpha_2$ , the maximum displacement is located at the middle position of the model.
- (ii) As  $\alpha_2$  increases from  $0^\circ$  to  $90^\circ$ , the average displacement on the model surface shows a variation trend of first decrease and then increase, reaching the minimum value at  $\alpha_2 = 45^\circ$ . When  $\alpha_2$  increases from  $0^\circ$  to  $45^\circ$ , the average displacement just decreases by 6.99%, while for  $\alpha_2$  increasing from  $45^\circ$  from  $90^\circ$ , the average displacement increases by 44.97% (Fig. 15).

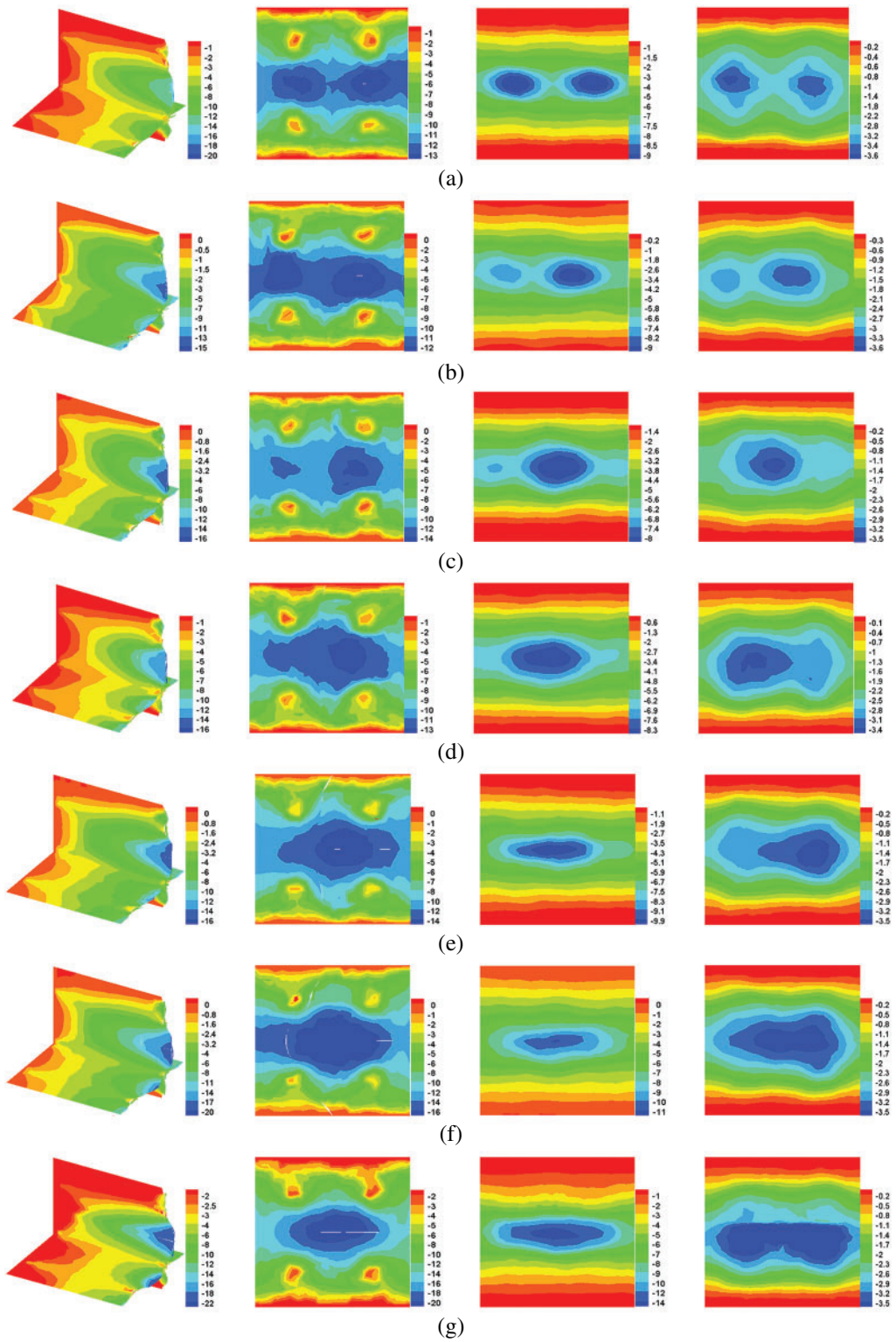


**Figure 14:** Displacement contours of the numerical models with various  $\alpha_2$  values. (a)  $\alpha_2 = 0^\circ$ . (b)  $\alpha_2 = 15^\circ$ . (c)  $\alpha_2 = 30^\circ$ . (d)  $\alpha_2 = 45^\circ$ . (e)  $\alpha_2 = 60^\circ$ . (f)  $\alpha_2 = 75^\circ$ . (g)  $\alpha_2 = 90^\circ$

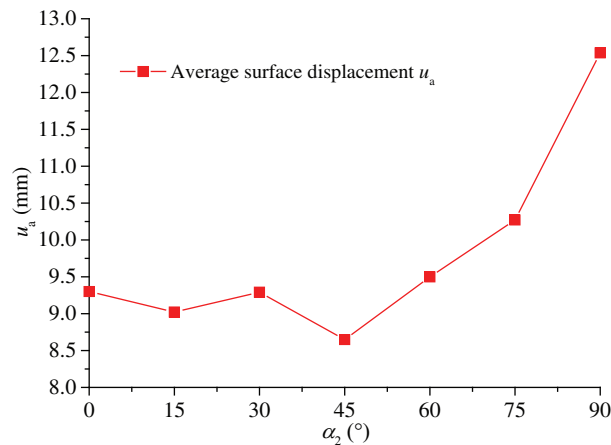


**Figure 15:** Variations in the average displacements of monitoring surfaces for the models with various  $\alpha_2$  values

Variations in the maximum principal stress contours of the monitoring surfaces with  $\alpha_2$  are displayed in Fig. 16. It can be seen that:

- (i) At the model surface, obvious stress concentration can be observed at the bolt position, and the stress decreases between two bolts, especially at the joint #3 position. With increasing  $\alpha_2$ , the stress concentration at joint #3 varies gradually. For  $\alpha_2 = 0^\circ$ , the stress reduction region is basically symmetrical. With increasing  $\alpha_2$  from  $15^\circ$  to  $60^\circ$ , the stress reduction region moves to right. For  $\alpha_2 = 90^\circ$ , the stress reduction region returns to the middle position again. The variation characteristics are generally consistent with the deformation changes discussed above.
- (ii) For a certain  $\alpha_2$ , obvious stress concentration is located at the bolt position, while at the free section of the bolt, a stress reduction phenomenon is generated, which also reflects the variations in the deformation and strength properties of the anchorage models.
- (iii) For  $\alpha_2 = 90^\circ$ , in the experiment, the secondary cracks of the anchorage model are more developed due to stress concentration near the bolt, which is consistent with the numerical results displayed in Fig. 16g, where the maximum principal stress at the bolt position is larger. Besides, due to bolt reinforcement, a shear failure of “X” shape is generated, which can also be verified in the displacement contour results in Fig. 14g.

### 3.4 Anchorage Properties of Blocky Rock Mass with Various $\beta_1$

Fig. 17a shows the axial stress-strain curves of anchorage blocky rock mass with various  $\beta_1$  values. It can be seen that, three different kinds of curves can be identified. For  $\beta_1 = 0^\circ$ , the stress-strain curve experiences the stages of elastic stage, plastic deformation stage, peak stress stage, strain-softening stage, second peak stress stage and residual strength stage. For  $\beta_1 = 30^\circ$ , the numerical model experiences the elastic stage, plastic deformation stage, stable stage, second strength stage, and residual strength stage. For  $\beta_1 = 15^\circ, 45^\circ, 60^\circ, 75^\circ$ , and  $90^\circ$ , the axial stress-strain curves experience the elastic deformation stage, plastic deformation stage, and stable stage.

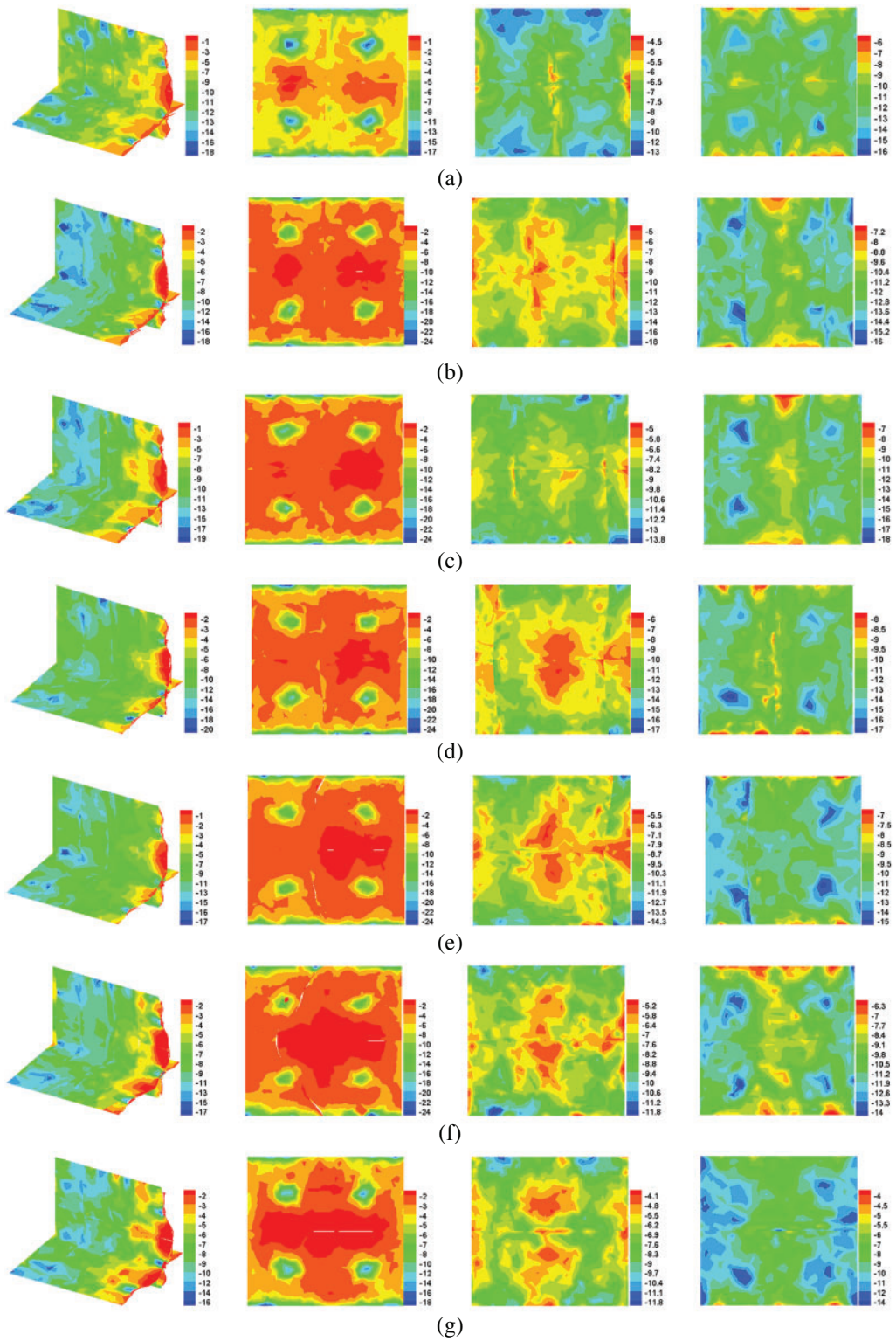


**Figure 16:** Maximum principal stress contours of the numerical models with various  $\alpha_2$  values. (a)  $\alpha_2 = 0^\circ$ . (b)  $\alpha_2 = 15^\circ$ . (c)  $\alpha_2 = 30^\circ$ . (d)  $\alpha_2 = 45^\circ$ . (e)  $\alpha_2 = 60^\circ$ . (f)  $\alpha_2 = 75^\circ$ . (g)  $\alpha_2 = 90^\circ$

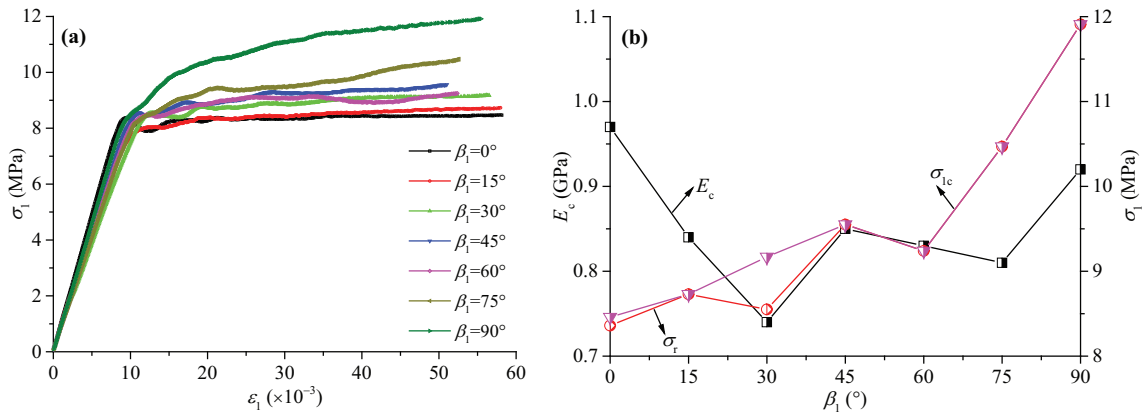


**Figure 17:** Axial stress-strain curves, elastic modulus and strength characteristics of the numerical models with various  $\beta_1$  values

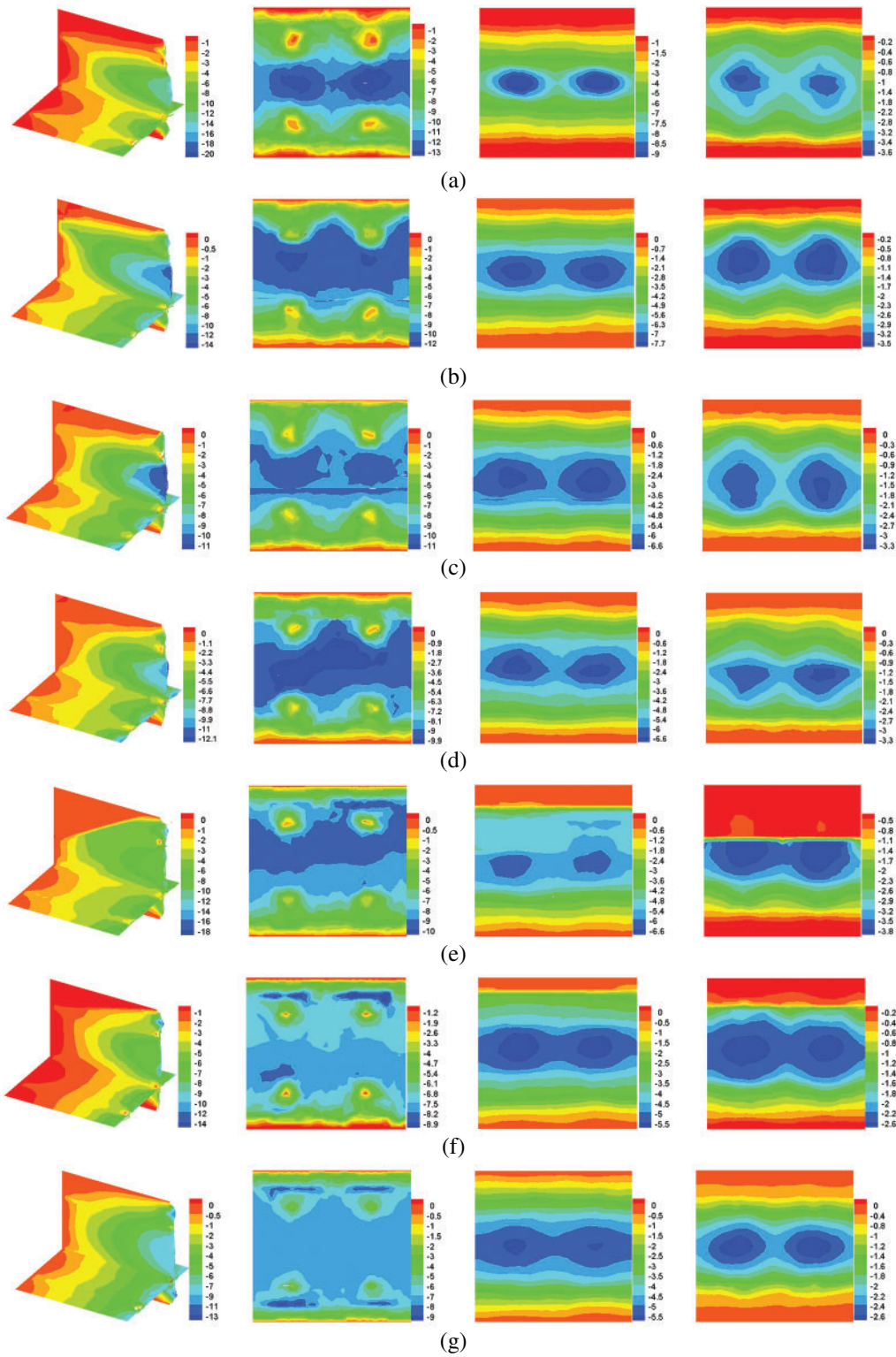
The mechanical properties of blocky rock mass with various  $\beta_1$  values are displayed in Fig. 17b. As  $\beta_1$  increases from  $0^\circ$  to  $90^\circ$ , the elastic modulus shows a first decrease and then increase variation, obtaining the minimum value of 0.74 GPa at  $\beta_1 = 30^\circ$ . Both the peak strength and residual strength increase gradually with increasing  $\beta_1$ , and the increase extent also shows an increase. However, the second peak strength just happens to  $\beta_1 = 0^\circ$  and  $30^\circ$ , and the second peak strength is larger than the peak strength  $\sigma_{1c}$ .

Variations in the average displacement contours of monitoring surfaces for the blocky rock mass with various  $\beta_1$  values are displayed in Figs. 18–19. It can be seen that:

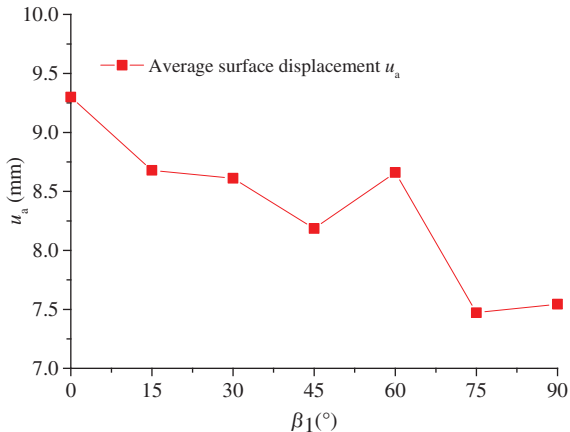
- (i) For  $\beta_1 = 0^\circ$ , the maximum deformation of the model surfaces happens between two bolts. With an increase in  $\beta_1$ , the maximum deformation position gradually transfers to the center and both ends of the model, e.g.,  $\beta_1 = 15^\circ$ ,  $30^\circ$  and  $45^\circ$ . When  $\beta_1$  is larger than  $60^\circ$ , the deformation far away from the bolt increases obviously due to variations in the blocky structures.
- (ii) The deformation distribution inside the model is basically the same, indicating the largest deformation in the middle steel belt position while small deformation at the model ends. With increasing  $\beta_1$ , the average surface displacement of the model generally shows a decreasing variation trend. However, for  $\beta_1 = 60^\circ$ , the average displacement undergoes an obvious increase, which is mainly due to relatively large slip along the joints for  $\beta_1 = 60^\circ$ , but for larger  $\beta_1$  values, the joint surface direction is gradually parallel to the loading direction, leading to a decrease in the deformation but an increase in the shear resistance capacity.

The maximum principal stress contours on the monitoring surfaces for the models with various  $\beta_1$  values are distributed in Fig. 20. It can be seen that:

- (i) At the model surface, obvious stress concentration can be observed at the bolt position and both end surfaces of the model. However, due to superposition between the stress fields of joints and bolts, the stress concentration phenomenon near the bolts for  $\beta_1 = 30^\circ$ ,  $60^\circ$ ,  $75^\circ$  and  $90^\circ$  is not obvious.

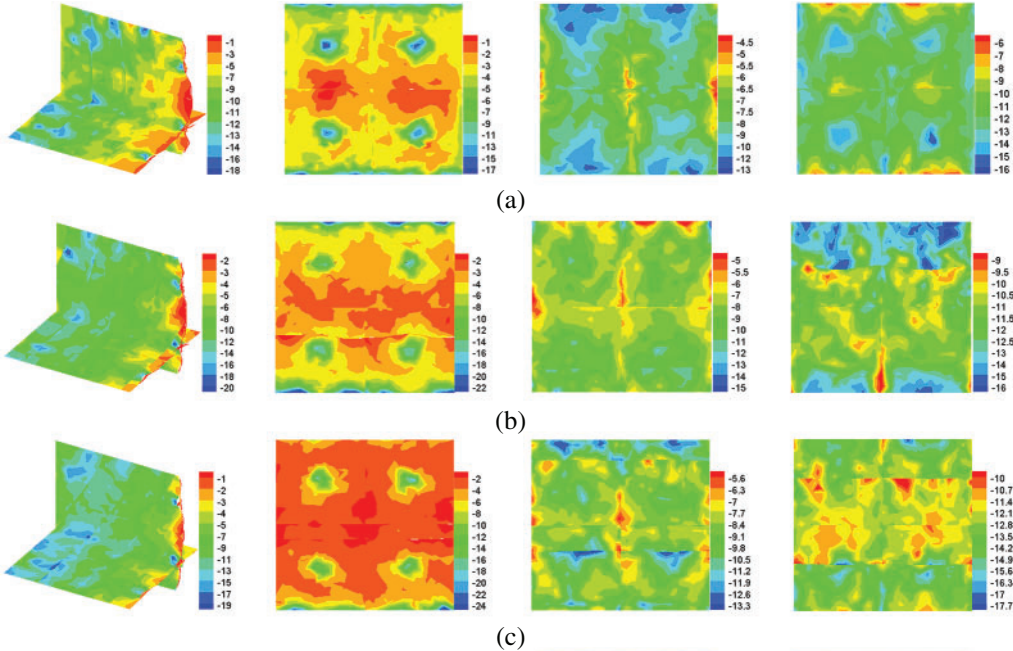


**Figure 18:** Displacement contours of the numerical models with various  $\beta_1$  values. (a)  $\beta_1 = 0^\circ$ . (b)  $\beta_1 = 15^\circ$ . (c)  $\beta_1 = 30^\circ$ . (d)  $\beta_1 = 45^\circ$ . (e)  $\beta_1 = 60^\circ$ . (f)  $\beta_1 = 75^\circ$ . (g)  $\beta_1 = 90^\circ$



**Figure 19:** Variations in the average displacements of monitoring surfaces for the models with various  $\beta_1$  values

(ii) At the free section of the bolt, the stress is mainly reduced on the vertical weak planes, but on the horizontal weak planes, both stress concentration and stress reduction can be observed. As  $\beta_1$  varies, the included angle between the joint surfaces and loading direction as well as the bolt direction varies, which results in changes in the stress distribution on the joint surfaces, leading to variations in the strength and deformation properties.



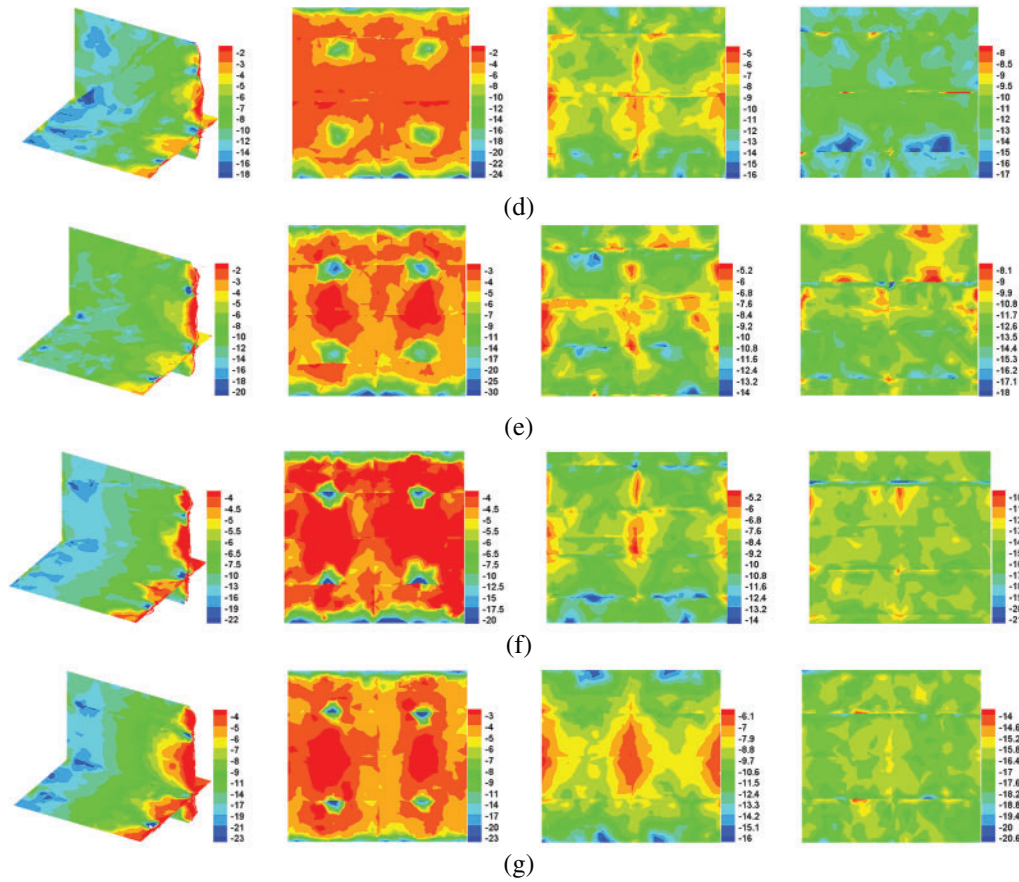


**Figure 20:** Maximum principal stress contours of the numerical models with various  $\beta_1$  values. (a)  $\beta_1 = 0^\circ$ . (b)  $\beta_1 = 15^\circ$ . (c)  $\beta_1 = 30^\circ$ . (d)  $\beta_1 = 45^\circ$ . (e)  $\beta_1 = 60^\circ$ . (f)  $\beta_1 = 75^\circ$ . (g)  $\beta_1 = 90^\circ$

From the numerical simulation results of anchorage models with various  $\alpha_1$ ,  $\alpha_2$  and  $\beta_1$  values discussed above, variations in  $\sigma_{1c}$ ,  $\sigma_{2c}$ ,  $\sigma_r$ , and  $E_c$  of the models with increasing dip angle  $\alpha_1$  and  $\alpha_2$  are similar. As  $\alpha_1$  or  $\alpha_2$  increases, the average displacement  $u_a$  presents a first decrease and then increase variation, achieving the minimum value at the angle of  $45^\circ$ . However, changes of the strength parameters of anchorage models with various  $\beta_1$  values are different, compared with the results of anchorage models with various  $\alpha_1$  and  $\alpha_2$  values. As  $\beta_1$  increases,  $u_a$  generally decreases. The above difference in strength and deformation parameters of the anchorage models with various  $\alpha_1$ ,  $\alpha_2$  and  $\beta_1$  values might be due to various included angles between the joint surfaces and the loading direction, as well as the anchorage direction of the bolt.

#### 4 Discussion

In the former experiment, ultimate failure modes of the anchorage rock mass can be characterized by shear or splitting failure. The shear failure is associated with shear resistance of both the rock matrix and structural planes, and the splitting failure is mainly associated with the cohesion force and internal frictional angle of both rock matrix and the structural planes. After bolt reinforcement, bearing capacity of the anchorage rock mass shows an obvious increase.

From the simplified mechanical unit shown in Fig. 2, the anchorage body is mainly affected by three directional stresses, i.e., vertical load  $\sigma_1$ , lateral restraint  $\sigma_2$  and the bolt effect  $\sigma_3$ , as listed in Tab. 3.

**Table 3:** Summary table of mechanical analysis for the structural planes

Joint surface	Normal stress	Shear stress	Failure condition
#1	$\sigma = \sigma_1 \cos \alpha + \sigma_3 \sin \alpha$	$\tau = \sigma_1 \sin \alpha - \sigma_3 \cos \alpha$	$\sigma_1 > \sigma_3 \left( \frac{1 + \mu^2}{\tan \alpha - \mu} + \mu \right)$
#2	$\sigma = \sigma_2 \cos \beta + \sigma_3 \sin \beta$	$\tau = \sigma_2 \sin \beta - \sigma_3 \cos \beta$	$\sigma_2 > \sigma_3 \left( \frac{1 + \mu^2}{\tan \beta - \mu} + \mu \right)$
#3	$\sigma = \sigma_1 \sin \gamma + \sigma_3 \cos \gamma$	$\tau = \sigma_1 \cos \gamma - \sigma_3 \sin \gamma$	$\sigma_1 > \sigma_3 \left( \frac{1 + \mu^2}{\mu (1 - \mu \tan \gamma)} - \frac{1}{\mu} \right)$

Notes:  $\alpha$ ,  $\beta$  and  $\gamma$  are dip angles of joint surfaces #1, #2 and #3, respectively.  $\mu$  is the frictional coefficient of the joint surfaces.

During the test, failure happens to the model when the tensile stress is larger than the tensile strength of the rock block, which can be discussed as follows:

- (i) The limit value of  $\sigma_3$  supplied by the bolt is constant. Thus, for dip angle  $\alpha, \beta > \arctan(\mu)$ , shear slip failure may happen on the joint surfaces, and when the joint dip angle increases, the required stress for the shear failure is smaller. However, for  $\gamma < \arctan(1/\mu)$ , with increasing dip angle, the stress required for the shear failure shows an increase, resulting in a larger bearing capacity.
- (ii) The strength properties of the joint surfaces are closely related to the imposed normal stress. For  $\alpha < \arctan(\sigma_3/\sigma_1)$  and  $\beta < \arctan(\sigma_2/\sigma_1)$ , with increasing dip angle of the joint surfaces, the normal stress acting on the structural planes increases continuously, resulting in increasing bearing capacity of the joints. However, for  $\gamma < \arctan(\sigma_1/\sigma_3)$ , due to much larger  $\sigma_1$  than  $\sigma_3$ ,  $\arctan(\sigma_1/\sigma_3)$  is close to  $90^\circ$ . Thus, as the dip angle increases, the normal stress imposed on the joint surfaces increases continuously, resulting in gradually increasing bearing capacity of the model.
- (iii) When the included angle between joint surfaces and the bolt direction is larger, the anchorage reinforcement of the bolt is more obvious. However, when the bolt is parallel to the joint surfaces, the bolt has little effect on the structural planes. On the one hand, the role of the bolt support is to make the rock mass three-dimensional stress state through compression effect, and on the other hand, the compression effect improves both the tensile strength and shear resistance of the joint surfaces.

## 5 Conclusions

In this study, both anchorage strength and deformation properties of the blocky rock mass were experimentally and numerically investigated. The main conclusions can be drawn as follows:

- (1) Due to bolt reinforcement, after the peak strength, axial stress of the anchorage model fluctuates within a certain range, implying typical strain-hardening characteristics, and the peak strength and elastic modulus increase by 21.56% and 20.0%, respectively. The

lateral strain generally undergoes three stages of no increase, rapid increase and attaining stable values, and the restriction effect of the bolt declines the deformation of the model surfaces.

- (2) With increasing  $\alpha_1$  from  $0^\circ$  to  $90^\circ$ , both the elastic modulus and surface displacement first decrease and then increase, while the peak strength, second peak strength and residual strength first increase and then decrease. With increasing  $\alpha_2$  from  $0^\circ$  to  $90^\circ$ , the elastic modulus of the anchorage models keeps generally constant, while the peak strength, second peak strength and residual strength first increase and then decrease. The surface displacement first decreases and then increases. With increasing  $\beta_1$  from  $0^\circ$  to  $90^\circ$ , the elastic modulus first decreases and then increases, while both the peak strength and second peak strength show a continuous increasing variation. The surface displacement gradually decreases.
- (3) Due to the effects of bolt reinforcement, cone-shaped compression zones are generated in the model, and the compression zones of adjacent bolts superimpose with each other to form anchorage belts, which improves the overall bearing capacity of anchorage structures. Obvious stress concentration can be observed at both the bolt end and anchorage section. Due to variations in the included angle between joint surfaces and the bolt direction, the maximum principle stress fields vary. The bolt reinforcement effects improve the normal stress of structural planes, which enhances the strength properties of both joint surfaces and the overall rock mass, especially the shear resistance.

**Funding Statement:** This work is financially supported by National Natural Science Foundation of China (Nos. 51904290, 51734009), Natural Science Foundation of Jiangsu Province, China (No. BK20180663), and Opening Fund of State Key Laboratory of Geohazard Prevention and Geoenvironment Protection (Chengdu University of Technology), China (No. SKLGP2020K021).

**Conflicts of Interest:** The authors declare that they have no conflicts of interest to report regarding the present study.

## References

1. Bauer, J. F., Meier, S., Philipp, S. L. (2015). Architecture, fracture system, mechanical properties and permeability structure of a fault zone in lower Triassic sandstone, Upper Rhine Graben. *Tectonophysics*, 647–648, 132–145. DOI 10.1016/j.tecto.2015.02.014.
2. Yin, Q., Jing, H., Su, H., Zhao, H. (2018). Experimental study on mechanical properties and anchorage performances of rock mass in the fault fracture zone. *International Journal of Geomechanics*, 18(7), 04018067. DOI 10.1061/(ASCE)GM.1943-5622.0001187.
3. Kong, L. W., Zeng, Z. X., Bai, W., Wang, M. (2018). Engineering geological properties of weathered swelling mudstones and their effects on the landslides occurrence in the Yanji section of the Jilin-Hunchun high-speed railway. *Bulletin of Engineering Geology and the Environment*, 77(4), 1491–1503. DOI 10.1007/s10064-017-1096-2.
4. Feng, G., Kang, Y., Wang, X., Hu, Y., Li, X. (2020). Investigation on the failure characteristics and fracture classification of shale under brazilian test conditions. *Rock Mechanics and Rock Engineering*, 53(7), 3325–3340. DOI 10.1007/s00603-020-02110-6.
5. Liu, R., He, M., Huang, N., Jiang, Y., Yu, L. (2020). Three-dimensional double-rough-walled modeling of fluid flow through self-affine shear fractures. *Journal of Rock Mechanics and Geotechnical Engineering*, 20(1), 41–49. DOI 10.1016/j.jrmge.2019.09.002.
6. Liu, R., Lou, S., Li, X., Han, G., Jiang, Y. (2020). Anisotropic surface roughness and shear behavior of rough-walled plaster joints under constant normal load and constant normal

- stiffness conditions. *Journal of Rock Mechanics and Geotechnical Engineering*, 12(2), 338–352. DOI 10.1016/j.jrmge.2019.07.007.
7. Fan, J., Liu, W., Jiang, D., Chen, J., Tiedeu, W. N. et al. (2020). Time interval effect in triaxial discontinuous cyclic compression tests and simulations for the residual stress in rock salt. *Rock Mechanics and Rock Engineering*, 53(9), 4061–4076. DOI 10.1007/s00603-020-02150-y.
  8. Wong, R. H. C., Lin, P., Tang, C. A., Chau, K. T. (2002). Creeping damage around an opening in rock-like material containing non-persistent joints. *Engineering Fracture Mechanics*, 69(17), 2015–2027. DOI 10.1016/S0013-7944(02)00074-7.
  9. Chen, H., Qin, S., Xue, L., Yang, B., Zhang, K. (2018). A physical model predicting instability of rock slopes with locked segments along a potential slip surface. *Engineering Geology*, 242, 34–43. DOI 10.1016/j.enggeo.2018.05.012.
  10. He, Z., Wang, B. (2018). Instability process model test for bedding rock slope with weak inter-layer under different rainfall conditions. *Advances in Civil Engineering*, 2018(8), 1–8. DOI 10.1155/2018/8201031.
  11. Hu, S., Tan, Y., Zhou, H., Ru, W., Ning, J. et al. (2020). Anisotropic modeling of layered rocks incorporating planes of weakness and volumetric stress. *Energy Science & Engineering*, 8(3), 789–803. DOI 10.1002/ese3.551.
  12. Wu, J., Feng, M., Mao, X., Xu, J., Zhang, W. et al. (2018). Particle size distribution of aggregate effects on mechanical and structural properties of cemented rockfill: experiments and modeling. *Construction and Building Materials*, 193, 295–311. DOI 10.1016/j.conbuildmat.2018.10.208.
  13. Ren, D., Zhou, D., Liu, D., Dong, F., Ma, S. et al. (2019). Formation mechanism of the Upper Triassic Yanchang formation tight sandstone reservoir in Ordos basin—take Chang 6 reservoir in Jiyuan oil field as an example. *Journal of Petroleum Science and Engineering*, 178, 497–505. DOI 10.1016/j.petrol.2019.03.021.
  14. Saadat, M., Taheri, A. (2020). Effect of contributing parameters on the behaviour of a bolted rock joint subjected to combined pull-and-shear loading: a DEM approach. *Rock Mechanics and Rock Engineering*, 53(1), 383–409. DOI 10.1007/s00603-019-01921-6.
  15. Xing, Y., Kulatilake, P. H. S. W., Sandbak, L. A. (2018). Effect of rock mass and discontinuity mechanical properties and delayed rock supporting on tunnel stability in an underground mine. *Engineering Geology*, 238, 62–75. DOI 10.1016/j.enggeo.2018.03.010.
  16. Chen, C., Peng, S., Wu, S., Xu, J. (2019). The effect of chemical erosion on mechanical properties and fracture of sandstone under shear loading: an experimental study. *Scientific Reports*, 9(1), 37. DOI 10.1038/s41598-019-56196-2.
  17. Shan, P., Lai, X. (2020). An associated evaluation methodology of initial stress level of coal-rock masses in steeply inclined coal seams, Urumchi coal field, China. *China Engineering Computations*, 37(6), 2177–2192. DOI 10.1108/EC-07-2019-0325.
  18. Zhang, X., Jiang, Y., Wang, G., Liu, J., Wang, D. et al. (2019). Mechanism of shear deformation, failure and energy dissipation of artificial rock joint in terms of physical and numerical consideration. *Geosciences Journal*, 23(3), 519–529. DOI 10.1007/s12303-018-0043-y.
  19. Wang, H., Lin, H. (2018). Non-linear shear strength criterion for a rock joint with consideration of friction variation. *Geotechnical & Geological Engineering*, 36(6), 3731–3741. DOI 10.1007/s10706-018-0567-y.
  20. Yang, W., Zhang, Q., Ranjith, P. G., Yu, R., Luo, G. et al. (2019). A damage mechanical model applied to analysis of mechanical properties of jointed rock masses. *Tunnelling and Underground Space Technology*, 84, 113–128. DOI 10.1016/j.tust.2018.11.004.
  21. Wang, Y., Tang, J., Dai, Z., Yi, T. (2018). Experimental study on mechanical properties and failure modes of low-strength rock samples containing different fissures under uniaxial compression. *Engineering Fracture Mechanics*, 197, 1–20. DOI 10.1016/j.engfracmech.2018.04.044.
  22. Malmgren, L., Nordlund, E. (2008). Interaction of shotcrete with rock and rock bolts—a numerical study. *International Journal of Rock Mechanics & Mining Sciences*, 45(4), 538–553. DOI 10.1016/j.ijrmms.2007.07.024.

23. Jing, H. W., Yang, S. Q., Zhang, M. L., Xu, G. A., Chen, K. F. (2014). An experimental study on anchorage strength and deformation behavior of large-scale jointed rock mass. *Tunnelling and Underground Space Technology*, 43, 184–197. DOI 10.1016/j.tust.2014.05.006.
24. Zhu, H., Xu, Q., Ding, W., Huang, F. (2011). Experimental study on the progressive failure and its anchoring effect of weak-broken rock vertical slope. *Frontiers of Architecture & Civil Engineering in China*, 5(2), 208–224. DOI 10.1007/s11709-011-0111-0.
25. Li, Y., Li, C., Zhang, L., Zhu, W., Li, S. et al. (2017). An experimental investigation on mechanical property and anchorage effect of bolted jointed rock mass. *Geosciences Journal*, 21(2), 253–265. DOI 10.1007/s12303-016-0043-8.
26. Wu, X., Jiang, Y., Gong, B., Guan, Z., Deng, T. (2019). Shear performance of rock joint reinforced by fully encapsulated rock bolt under cyclic loading condition. *Rock Mechanics and Rock Engineering*, 53(8), 2681–2690. DOI 10.1007/s00603-018-1698-4.
27. Fardin, N., Stephansson, O., Jing, L. (2001). The scale dependence of rock joint surface roughness. *International Journal of Rock Mechanics and Mining Sciences*, 38(5), 659–669. DOI 10.1016/S1365-1609(01)00028-4.
28. Fardin, N. (2008). Influence of structural non-stationarity of surface roughness on morphological characterization and mechanical deformation of rock joints. *Rock Mechanics and Rock Engineering*, 41(2), 267–297. DOI 10.1007/s00603-007-0144-9.
29. Ueng, T. S., Jou, Y. J., Peng, I. H. (2010). Scale effect on shear strength of computer-aided-manufactured joints. *Journal of Geoengineering*, 5(2), 29–37.
30. Roy, D. G., Singh, T. N., Kodikara, J., Das, R. (2017). Effect of water saturation on the fracture and mechanical properties of sedimentary rocks. *Rock Mechanics and Rock Engineering*, 50(10), 2585–2600. DOI 10.1007/s00603-017-1253-8.
31. Song, X., Li, X., Li, Z., Cheng, F., Zhang, Z. et al. (2018). Experimental research on the electromagnetic radiation (EMR) characteristics of cracked rock. *Environmental Science and Pollution Research*, 25(7), 6596–6608. DOI 10.1007/s11356-017-1012-0.
32. Zhang, H., Elsworth, D., Wan, Z. (2018). Failure response of composite rock-coal samples. *Geomechanics and Geophysics for Geo-Energy and Geo-Resources*, 4(2), 175–192. DOI 10.1007/s40948-018-0082-x.
33. Amarasiri, A., Kodikara, J. (2011). Use of material interfaces in DEM to simulate soil fracture propagation in mode I cracking. *International Journal of Geomechanics*, 11(4), 314–322. DOI 10.1061/(ASCE)GM.1943-5622.0000090.
34. Tan, X., Li, W., Zhao, M., Tam, V. W. Y. (2019). Numerical discrete-element method investigation on failure process of recycled aggregate concrete. *Journal of Materials in Civil Engineering*, 31(1), 1–14.
35. Deng, X. F., Zhu, J. B., Chen, S. G., Zhao, J. (2012). Some fundamental issues and verification of 3DEC in modeling wave propagation in jointed rock masses. *Rock Mechanics and Rock Engineering*, 45(5), 943–951. DOI 10.1007/s00603-012-0287-1.
36. Wu, J. H., Lin, W. K., Hu, H. T. (2018). Post-failure simulations of a large slope failure using 3DEC: the Hsien-du-shan slope. *Engineering Geology*, 242, 92–107. DOI 10.1016/j.enggeo.2018.05.018.
37. Vermeer, P. A., deBorst, R. (1984). Non-associated plasticity for soils, concrete and rock. *Heron*, 29(3), 3–62.
38. Meng, B., Jing, H. W., Yang, X. X., Chen, K. F., Yang, S. Q. (2013). Experimental study of deformation and failure characteristics of anchorage unit in fractured surrounding rocks. *Chinese Journal of Rock Mechanics & Engineering*, 32(12), 2497–2505.
39. Wang, C. X., Shen, B. T., Chen, J. T., Tong, W. X., Jiang, Z. et al. (2020). Compression characteristics of filling gangue and simulation of mining with gangue backfilling: an experimental investigation. *Geomechanics and Engineering*, 20(6), 485–495.
40. Peng, H., Fan, J., Zhang, X., Chen, J., Li, Z. et al. (2020). Computed tomography analysis on cyclic fatigue and damage properties of rock salt under gas pressure. *International Journal of Fatigue*, 134(5), 105523–105532. DOI 10.1016/j.ijfatigue.2020.105523.

41. Yin, Q., Ma, G., Jing, H., Wang, H., Su, H. et al. (2017). Hydraulic properties of 3D rough-walled fractures during shearing: an experimental study. *Journal of Hydrology*, 555, 169–184. DOI 10.1016/j.jhydrol.2017.10.019.
42. Wu, G., Jia, S., Chen, W., Yuan, J., Yu, H. et al. (2018). An anchorage experimental study on supporting a roadway in steeply inclined geological formations. *Tunnelling and Underground Space Technology*, 82(12), 125–134. DOI 10.1016/j.tust.2018.08.007.